


Article

The Space-Time Properties of Three Static Black Holes

Yu Wang ^{1,*} , Gangqi Shen ¹ and Xin Sun ²

¹ Guangxi Key Laboratory for Relativistic Astrophysics, School of Physical Science and Technology, Guangxi University, Nanning 530004, China

² Department of Physics and Astronomy, Sun Yat-sen University, Zhuhai 519082, China

* Correspondence: 2107401023@st.gxu.edu.cn

Abstract: In the curved space-time, the neutral test particle is not affected by any other force except for the influence of the curved space-time. Similar to the free sub in the flat space, the Lagrangian of the test particle only contains the kinetic energy term—the kinetic energy term of the four-dimensional curved space-time. In the case of small space-time curvature, linear approximation can be made. That is, under the weak field approximation, the Lagrangian quantity degenerates into the Lagrangian quantity in the axisymmetric gravitational field in Newtonian mechanics. In this paper, the curved space-time composed of axisymmetric equidistant black holes is taken as a model. We study the geodesic motion of the test particles around three black holes with equal mass and static axisymmetric distribution, including time-like particles and photons. The three extreme Reissner–Nordstrom black holes are balanced by electrostatic and gravitational forces. We first give the geodesic motion equation of particles in Three black holes space-time, give the relativistic effective potential, discuss the possible motion state of particles, and classify their motion trajectories. Then, the particle motion of the special plane (equatorial plane) is studied. The circular orbits of the two types of particles in the symmetric plane are studied, respectively. The circular orbits outside the symmetric plane are also studied, and their stability is also discussed. We will show the influence of the separation distance of the three black holes on the geodesic motion and explore the change of the relativistic effective potential. Then, the relationship between the inherent quantity and the coordinate quantity in space-time is analyzed. Finally, the chaos of the test particle orbit is explored.

Keywords: effective potential; RN black holes; chaos; test particle; curved space-time



Citation: Wang, Y.; Shen, G.; Sun, X. The Space-Time Properties of Three Static Black Holes. *Symmetry* **2023**, *15*, 702. <https://doi.org/10.3390/sym15030702>

Academic Editor: Grant J. Mathews

Received: 25 December 2022

Revised: 23 February 2023

Accepted: 6 March 2023

Published: 11 March 2023



Copyright: © 2023 by the authors. Licensee MDPI, Basel, Switzerland. This article is an open access article distributed under the terms and conditions of the Creative Commons Attribution (CC BY) license (<https://creativecommons.org/licenses/by/4.0/>).

1. Introduction

In curved space-time, the motion of the test particle is entirely determined by the space-time metric. In cases where the curvature of spacetime is not obvious, that is, in a weak field, such as our own in the solar system, we usually think of it as flat spacetime. Classical mechanics was sufficient to explain most phenomena, and Newton's gravitation was used to explain the motion of the planets, a very good approximation, with great success. However, essentially the motion of the planets is determined by the nature of the four-dimensional space-time around the sun that is curved by the sun.

The study of black hole theory is not perfect so far. On one hand, because the classical theory ignores the quantum effect in the small scale, the black hole theory itself is still developing and improving. On the other hand, due to the unidirectional membrane characteristics of the black hole, it is difficult to obtain direct observation data, it is mainly to infer the existence of objects that conform to the characteristics of black holes by observing the abnormal behavior of surrounding stars. However, with the discovery of ultra-dense celestial neutron stars, scientists became convinced that black holes were abundant in the universe because the degenerate neutron pressure of a neutron star greater than 3.2 solar masses was no longer strong enough to resist gravity and would collapse into a black hole. In fact, in 2015, LIGO detected gravitational waves from a binary black hole [1,2]. This observation confirmed the existence of a binary black hole system in nature [3,4]. So

far, 10 black hole mergers and one neutron star merger have been detected, with more to come. These findings have given a powerful impetus to the study of the phenomenon of binary black hole systems. The actual binary black hole systems are dynamic and it is useful to describe the phenomena in these systems by means of numerical relativity. On the other hand, it is also important to use analytical methods to understand these phenomena qualitatively. However, due to the dynamic characteristics of the binary black hole system, there is no analytical expression for it. Therefore, we often use static (or static) and axisymmetric binary black hole space-time as models. Einstein equations (or Einstein–Maxwell equations) have a number of binary black hole solutions with these symmetries, which are Weyl space-time [5] or Majumdar–Papapetrou (MP) space-time [6–8], the double Kerr space-time [9], etc. We can learn a lot from such space-time phenomena. For example, although the formation of binary black hole shadows requires a completely nonlinear numerical relativistic simulation, we can use the (quasi-static) space-time of binary black holes to identify certain characteristics [10–15]. The study of measuring particle motion in strong gravitational fields is of great significance in astrophysics and gravity theory. Even in a binary black hole system, it remains one of the most fundamental problems. In fact, the formation of these black hole shadows is a matter of massless particle dynamics. Binary black hole systems in the universe are highly dynamic systems without analytical solutions. Therefore, a numerical calculation method is needed to analyze the geodesic motion around these systems to obtain the numerical solutions of the test particles. On the other hand, the dynamics of a large number of particles in a binary black hole system have been discussed in the context of gravitational wave radiation caused by the third object effect [16–19] and the formation of multiple accretion disks [20,21]. Among these phenomena, a stable circular orbital sequence is crucial, especially the innermost stable circular orbit (ISCO), which is considered to be the inner edge of an accretion disk [22]. Additionally, an inspiralling compact binary transits into the merging phase there [23,24]. There is also much research on the binary immovable black holes as follows: Chandrasekhar as early as 1989 [25] had studied radiation scattering from the two extremes of the RN black hole. These are the two fixed central problems of classical mechanics, which have many applications in celestial mechanics, and the main interest of this problem is that it is classically integrable, but in relativity it is not integrable, and the system is chaotic. In 1990 and 1991 [26,27], Contopoulos studied the ordered and chaotic geodesic orbits of particles around the double stationary black holes. Others studied the circular orbits of two black holes of equal mass in the equatorial plane and the circular orbits outside the symmetric plane [28]. This paper [29] studies the bound orbits of particles around a single rotating black ring. It is proved that there are stable helical orbits near the “axis” of the ring, and in special cases, stable circular orbits on the axis. If the ring thickness is less than a critical value, the stable bound orbit can have arbitrarily large dimensions. The bound orbits of free particles around a single rotating black ring are studied. Using the Poincaré diagram, we find that there are chaotic motions of particles bound by gravity to the black ring [30]. The geodesic motion of massless particles in a single rotating black ring is studied. When the thickness parameter of the black ring is less than the critical value, the stable geostationary orbit of the ring-helical massless particle is found. In addition, there are non-stationary massless particles in the finite region beyond the horizon. This is the first example of a massless particle in a stable constrained orbit around a black object [31].

The study of ISCO is of great importance, for three reasons. First, the geometry of space-time can be reflected by the innermost stable circular orbit reaction of the particle. Second, a binary system of test particles and a black hole can be a source of gravitational waves [32–34]. More importantly, the study of ISCO allows us to understand accretion disks and the associated radiation spectrum [35,36]. For a massive particle with no charge and no spin, we know that the radius of its ISCO is $6M$, and M is the mass of the black hole when it re-orbits the Schwarzschild black hole [37]. The ISCO radius of a RN black hole ranges from $4m$ (corresponding to an extreme black hole) to $6m$ (corresponding to the Schwarzschild limit) [38]. Things become a little more complicated when particles

move around the Kerr black hole. Under the background of an extreme Kerr black hole, the $r_{ISCO} = M$ of the co-rotating orbit and $r_{ISCO} = 9M$ of the reverse rotating orbit [39]. The ISCO study of Kerr–Newman (KN) black holes can be seen as a combination of the RN case and the Kerr case [40]. Other studies on ISCO can be found in the literature [41–66], including the motion of charged particles around the KN black hole [67]. In fact, a classical test particle might have spin angular momentum. The papers [68,69] studied the influence of spin on the orbits of ISCO in Schwarzschild black holes, [69,70] studied the influence of spin on the orbits of ISCO in Kerr black holes, and [71] studied the influence of spin on the orbits of ISCO in KN black holes. In addition, the study of particle motion near the black hole can also provide a valuable reference for the study of astrophysical events [44] and high-energy events [72] related to the black hole.

This paper is organized as follows, in Section 2, there are many different configurations of three stationary black holes, equidistant collinear, unequal collinear, equilateral triangle, isosceles triangle, general triangle, etc. We select axisymmetric coordinate system, according to the test amount of relativity Lagrangian particle, starting from the Lagrange equation, this paper derived the space-time three black holes (TBH) class particles and photons geodesic equation of motion, and according to several conservation quantity, effective potential energy is given, and on the symmetry plane of the particle orbit are classified, and then gives the symmetry plane of Hamilton canonical equation. Of course, in this section we have calculated the expressions of the fundamental geometric quantities in TBH spacetime and even discussed the event horizon problem. In Section 3, we discuss the effect of mass ratio on effective potential. In Section 4, we use the phase plane analysis method to discuss the stability of symmetric plane orbits and give the constraint conditions. In Section 5, we give the conditions satisfied by the stable circular orbit in TBH space-time, and give the space-time stability region diagram under specific parameters. In Section 6, we derive the gravitational red shift expression of TBH space-time and give the relationship between the coordinate quantity and the intrinsic quantity. In Section 7, we discuss the chaotic properties of the test particle in this space-time. In Section 8, we summarize the conclusion of the article.

2. Space-Time Metric and Equations of Motion

2.1. TBH Space-Time Metric

The general Reissner–Nordström metric expression is as follows:

$$ds^2 = - \left(1 - \frac{2M}{r} + \frac{Q^2}{r^2} \right) dt^2 + \left(1 - \frac{2M}{r} + \frac{Q^2}{r^2} \right)^{-1} dr^2 + r^2 (d\theta^2 + \sin^2 \theta d\phi^2). \quad (1)$$

For a black hole with a mass of M and a charge of $|Q|=M$, the black hole is called an extreme black hole, and its space-time metric can be simplified as:

$$ds^2 = - \left(1 - \frac{M}{r} \right)^2 dt^2 + \left(1 - \frac{M}{r} \right)^{-2} dr^2 + r^2 (d\theta^2 + \sin^2 \theta d\phi^2). \quad (2)$$

In isotropic coordinates ($\bar{r} \equiv r - M$), we can further simplify:

$$ds^2 = - \left(1 + \frac{M}{\bar{r}} \right)^{-2} dt^2 + \left(1 + \frac{M}{\bar{r}} \right)^2 (\beta) \quad (3)$$

$$\beta = [d\bar{r}^2 + \bar{r}^2 (d\theta^2 + \sin^2 \theta d\phi^2)]. \quad (4)$$

where β is the Euclidean flat metric. It is not difficult to find that the metric function $1 + M/\bar{r}$ in Equation (2) satisfies the Laplace equation in space and has the form of a harmonic

function in Euclidean space. Surprisingly, when $1 + M/\bar{r}$ is replaced by a more general harmonic function, the metric of Equation (3) is still the solution to the Einstein–Maxwell equations. This is the metric first discovered by Majumdar and Papapetrou [6–8], and we will talk about this space-time.

The Majumdar–Papapetrou space-time metric has the following form:

$$ds^2 = -U^{-2}(\vec{r})dt^2 + U^2(\vec{r})d\vec{r} \cdot d\vec{r}, \tag{5}$$

$$d\vec{r} \cdot d\vec{r} = dx^2 + dy^2 + dz^2, \tag{6}$$

$$R_{\mu\nu} - \frac{1}{2}g_{\mu\nu}R = \kappa T_{\mu\nu}. \tag{7}$$

When solving equations, $T_{\mu\nu} = 0$. The U here satisfies the Einstein field Equation (7), which can be directly reduced to the Laplace Equation (8).

$$\nabla^2 U = \frac{\partial^2 U}{\partial x^2} + \frac{\partial^2 U}{\partial y^2} + \frac{\partial^2 U}{\partial z^2} = 0. \tag{8}$$

The corresponding solution was given in Hawking’s paper [8]:

$$U(x) = 1 + \sum_i \frac{m_i}{r_i}, \tag{9}$$

$$r_i = \left[(x - x_i)^2 + (y - y_i)^2 + (z - z_i)^2 \right]^{\frac{1}{2}}. \tag{10}$$

where i goes from 1 to 3. Here, \vec{r} represents the position vector in the plane of three-dimensional space, which is called the background space. For example, in Cartesian coordinates, $\vec{r} = (x, y, z)$. In the subsequent theoretical analysis, an appropriate coordinate system should be selected according to the model for the convenience of calculation. Here, it is more appropriate to select column coordinates for TBH space-time. TBH space-time itself has spatial rotation symmetry. Here, we choose cylindrical coordinate system so that there can be more cyclic coordinates. The metric and the gauge field of the TBH spacetime in isotropic coordinates are given by:

$$ds^2 = g_{\mu\nu}dx^\mu dx^\nu = \frac{-dt^2}{U^2} + U^2(d\rho^2 + \rho^2 d\phi^2 + dz^2). \tag{11}$$

For the convenience of subsequent calculations, the covariant components of the metric are listed:

$$g_{tt} = -U^{-2}. \tag{12}$$

$$g_{\rho\rho} = U^2. \tag{13}$$

$$g_{\phi\phi} = U^2 \rho^2. \tag{14}$$

$$g_{zz} = U^2. \tag{15}$$

$$A_\mu dx^\mu = A^\nu g_{\mu\nu} dx^\mu = \Phi U^{-2} dt = U^{-1} dt. \tag{16}$$

$$\Phi(\vec{r}) = U(\vec{r}). \tag{17}$$

Equation (17) shows that electrostatic potential is equal to gravitational potential. In the space-time satisfying this equation, the position of the black hole can be arbitrarily placed. As long as the black hole has the same charge, these black holes can be relatively static, thus forming the static space-time. After coordinate transformation, we give the specific expression of U in a cylindrical coordinate system.

$$U(\rho, z) = 1 + \frac{M_1}{\sqrt{\rho^2 + (z - a)^2}} + \frac{M_2}{\sqrt{\rho^2 + (z + a)^2}} + \frac{M_3}{\sqrt{\rho^2 + z^2}}, \tag{18}$$

where M_i ($i = 1, 2, 3$) are masses of three extremal Reissner–Nordström black holes, M_1, M_2 are located at $z = \pm a$ ($a \geq 0$), and M_3 is located at $z = 0$. Note that we choose cylindrical coordinates on the spatial geometry, $x = \rho \cos \phi$ and $y = \rho \sin \phi$, where x and y are the Cartesian coordinates.

2.2. Test Particle Motion Equation

The Lagrangian of a flat space-time free particle is

$$\mathcal{L} = \frac{1}{2}m\dot{v}^2. \tag{19}$$

Through such an analogy, it can be seen that the Lagrangian of the freely tested particles in curved space-time is:

$$\mathcal{L} = \frac{1}{2}g_{\mu\nu}\dot{x}^\mu\dot{x}^\nu = \frac{1}{2}\left[-\frac{\dot{t}^2}{U^2} + U^2(\dot{\rho}^2 + \rho^2\dot{\phi}^2 + \dot{z}^2)\right]. \tag{20}$$

The point here is the derivative of the affine parameter. Since the TBH space-time is static axisymmetric, t and angular ϕ are not obvious in Lagrangian, resulting in the conservation of energy and angular momentum. Now we introduce a common killing vector to introduce two conserved quantities. Hypothesis:

$$\zeta^\mu = \delta^\mu_\nu. \tag{21}$$

Where the value of ν is determined. The infinitesimal mapping generated by this Killing vector is:

$$\tilde{x}^\mu = x^\mu, (\mu \neq \nu)\tilde{x}^\mu = x^\mu + \epsilon, (\mu = \nu). \tag{22}$$

The coordinate x^ν of the corresponding point has only changed by a small amount. This mapping is an equal metric mapping, which means that the metric field is independent of x^ν . In this case, we call x^ν the cyclic coordinates of the metric field, and when x^ν is the cyclic coordinates, the corresponding conserved quantities of the test particles are as follows:

$$p_\mu\zeta^\mu = p_\mu\delta^\mu_\nu = p_\nu. \tag{23}$$

Note that the conserved quantity is the corresponding component of the covariance quantity. Now, back in TBH space time, it is not difficult to find that t and ϕ are cyclic coordinates, so the conserved quantities of the moving particles are p_t and p_ϕ .

$$p_t = g_{t\nu}p^\nu = g_{tt}p^t = -\frac{1}{U^2}\dot{t} \tag{24}$$

$$p_\phi = g_{\phi\nu}p^\nu = g_{\phi\phi}p^\phi = \rho^2U^2\dot{\phi}. \tag{25}$$

$$E = \frac{\dot{t}}{U^2}, \quad L = \rho^2U^2\dot{\phi}. \tag{26}$$

where we may assume that $E > 0$. The Lagrangian equation is:

$$\frac{d}{dt}\frac{\partial L}{\partial \dot{q}_\alpha} - \frac{\partial L}{\partial q_\alpha} = 0. \tag{27}$$

Now we can write the equations of motion corresponding to z and ρ in the four space-time coordinates according to the Lagrange equation as follows:

$$U^2\ddot{z} - [t^2U^{-3} + U(\rho^2 + \rho^2\dot{\phi}^2 + \dot{z}^2)]U_z = 0. \tag{28}$$

$$U^2\ddot{\rho} - [U^2\dot{\phi}^2\rho + (U^{-3}\dot{t}^2 + U(\dot{\rho}^2 + \rho^2\dot{\phi}^2 + \dot{z}^2))U_\rho] = 0. \tag{29}$$

where U_z and U_ρ are partial derivatives of the potential energy function U with respect to the coordinates z and ρ .

2.3. Contact and Curvature

Of course, we could have given the equation of motion directly from the geodesic equation of motion (30), but we need to calculate in advance all the non-zero components of the Kirschner sign using the metric and the Christopher sign relation (31).

$$\ddot{x}^i + \Gamma_{jk}^i \dot{x}^j \dot{x}^k = 0 \tag{30}$$

$$\Gamma_{jk}^i(x) = \frac{1}{2}g^{il} \left(\frac{\partial g_{lk}}{\partial x^j} + \frac{\partial g_{jk}}{\partial x^l} - \frac{\partial g_{ik}}{\partial x^j} \right). \tag{31}$$

Now by comparing the coefficients of the equations of motion with the geodesic equations, we can calculate the non-zero points of all Christopher symbols at:

$$\Gamma_{t\rho}^t = -U^{-1}U_\rho \tag{32}$$

$$\Gamma_{tz}^t = -U^{-1}U_z \tag{33}$$

$$\Gamma_{\rho\phi}^\phi = U^{-1}U_\rho + \rho^{-1} \tag{34}$$

$$\Gamma_{z\phi}^\phi = U^{-1}U_z \tag{35}$$

$$\Gamma_{\rho z}^z = U^{-1}U_\rho \tag{36}$$

$$\Gamma_{tt}^z = -U^{-5}U_z \tag{37}$$

$$\Gamma_{\rho\rho}^z = -U_zU^{-1} \tag{38}$$

$$\Gamma_{\phi\phi}^z = -U_z\rho^2U^{-1} \tag{39}$$

$$\Gamma_{zz}^z = U_zU^{-1} \tag{40}$$

$$\Gamma_{tt}^\rho = -U^{-5}U_\rho \tag{41}$$

$$\Gamma_{\rho\rho}^\rho = U_\rho U^{-1} \tag{42}$$

$$\Gamma_{\phi\phi}^\rho = -(\rho + U_\rho\rho^2U^{-1}) \tag{43}$$

$$\Gamma_{\rho z}^\rho = U^{-1}U_\rho \tag{44}$$

$$\Gamma_{zz}^\rho = -U_\rho U^{-1}. \tag{45}$$

So far, we have found thirteen components of the TBH space-time connection, the rest of which are zero. The curvature tensor is an intrinsic property that reflects the degree of curvature in space-time, and with the Christopher symbol, the curvature tensor in Riemann space can be calculated. It is not only related to the planeness of space, but also an important indicator of the relative acceleration of two points in time and space, which can be reflected by the geodesic deviation equation. Their relationship is as follows:

$$R_{\lambda\mu\nu}^\rho = \Gamma_{\lambda\mu,\nu}^\rho - \Gamma_{\lambda\nu,\mu}^\rho + \Gamma_{\lambda\sigma\mu}^\rho \Gamma_{\lambda\nu}^\sigma - \Gamma_{\lambda\sigma\nu}^\rho \Gamma_{\lambda\mu}^\sigma \tag{46}$$

$$a^\mu = R_{\lambda\mu\nu}^\rho T^\lambda T^\nu S^\rho. \tag{47}$$

This equation, also known as the Jacobi equation, tells us that the relative acceleration between two geodesics is proportional to the curvature, where T^μ is the tangent vector of the geodesic, S^σ is the deviation vector, and a^μ is the four-dimensional acceleration. It can be seen that curvature is very important. We obtain 19 non-zero components in TBH space-time:

$$R^z_{tt\rho} = -6U^{-6}U_\rho U_z + U^{-5}U_{z\rho} \tag{48}$$

$$R^z_{ttz} = U_{zz}U^{-5} - 4U^{-6}U_z U_z \tag{49}$$

$$R^z_{\rho\rho z} = U^{-1}U_{\rho\rho} - U^{-1}U_{zz} - (2 + \rho^2)U_z^2 - U^{-1}U_\rho^2 \tag{50}$$

$$R^z_{\phi\phi\rho} = 2U^{-2}\rho^2 U_\rho U_z - 3U^{-1}\rho U_z^2 - (U^{-1}\rho^2 + U^{-2})U_{z\rho} \tag{51}$$

$$R^z_{\phi\phi z} = U_{zz}\rho^2 U^{-1} + U^{-2}\rho^2 U_z^2 + U^{-2}\rho^2 U_\rho^2 + U^{-1}\rho U_\rho \tag{52}$$

$$R^z_{\rho z\rho} = U^{-2}(U_z^2 - U_\rho^2) + U^{-1}(U_{\rho\rho} - U_{zz}) \tag{53}$$

$$R^z_{\rho z\phi} = -U^{-2}U_z U_\rho + 2U^{-1}U_{\rho z} + U^{-2}\rho^4 U_z^2 \tag{54}$$

$$R^t_{\rho t\rho} = -3U^{-2}U_\rho^2 + U^{-1}U_{\rho\rho} - U^{-2}U_z^2 \tag{55}$$

$$R^t_{\rho tz} = -U^{-2}U_\rho U_z + U^{-1}U_{\rho z} - 3U^{-2}U_z U_\rho \tag{56}$$

$$R^t_{zt\rho} = U^{-1}U_{z\rho} - 4U^{-2}U_z U_\rho \tag{57}$$

$$R^t_{ztz} = U^{-2}U_\rho^2 + U^{-1}U_{zz} - 3U^{-2}U_z^2 \tag{58}$$

$$R^\phi_{\rho\phi\rho} = -U^{-1}U_{\rho\rho} + 2U^{-2}U_\rho^2 - U^{-2}U_z^2 - \rho^{-1}U^{-1}U_\rho \tag{59}$$

$$R^\phi_{\rho\phi z} = -U^{-1}U_{z\rho} + U^{-2}U_\rho^2 + \rho^{-1}U^{-1}U_\rho + U^{-2}U_z U_\rho - \rho^{-1}U^{-1}U_z \tag{60}$$

$$R^\phi_{z\phi z} = U^{-2}U_z^2 - U^{-1}U_{zz} - U^{-2}U_\rho^2 - \rho^{-1}U^{-1}U_\rho \tag{61}$$

$$R^\phi_{z\phi\rho} = 2U^{-2}U_\rho U_z - U^{-1}U_{z\rho} \tag{62}$$

$$R^\rho_{zz\rho} = U^{-1}U_{z\rho} - U^{-2}(U_z^2 + U_\rho^2) \tag{63}$$

$$R^\rho_{tt\rho} = -3U^{-6}U_\rho^2 + U^{-5}U_{\rho\rho} - U^{-6}U_z^2 \tag{64}$$

$$R^\rho_{\phi\phi\rho} = -U^{-2}U_\rho^2 \rho^2 + U^{-1}\rho U_\rho + \rho^2 U_{\rho\rho} U^{-1} + \rho^2 U_z^2 U^{-2} \tag{65}$$

$$R^\rho_{\phi\phi z} = U_{\rho z}\rho^2 U^{-1} - 2U_\rho U_z \rho^2 U^{-2}. \tag{66}$$

After obtaining the curvature tensor, the Ricci tensor can be obtained by shrinking the index of the curvature tensor.

$$R_{\mu\nu} = R^\lambda_{\mu\lambda\nu}. \tag{67}$$

Then, we can calculate the curvature scalar according to the Ricci tensor we have obtained. Here we need to contract again. The order of the tensor will be 0 (scalar):

$$R = g^{\mu\nu} R_{\mu\nu} = R^\mu_\mu \tag{68}$$

$$R^\mu_\mu = R^t_t + R^\rho_\rho + R^\phi_\phi + R^z_z \tag{69}$$

$$R^t_t = g^{tt} R_{tt} \tag{70}$$

$$R^\rho_\rho = g^{\rho\rho} R_{\rho\rho} \tag{71}$$

$$R^\phi_\phi = g^{\phi\phi} R_{\phi\phi} \tag{72}$$

$$R^z_z = g^{zz} R_{zz}. \tag{73}$$

2.4. Hamiltonian Canonical Equation

According to the four velocity normalization, we have this relational expression: $g_{\mu\nu}\dot{x}^\mu\dot{x}^\nu = -\kappa$, where $\kappa = 1$ for time-like particles and $\kappa = 0$ for photons. Four motion integrals for the motion of the test particle in TBH space-time have been found, and they

are, respectively: $E, L, \kappa, z = 0$. Then we give the Hamiltonian for the test particle. First, we define the covariance:

$$P_\alpha = \frac{\partial \mathcal{L}}{\partial \dot{x}^\alpha} = g_{\alpha\beta} \dot{x}^\beta. \tag{74}$$

According to Legendre transformation, we can obtain the Hamiltonian from Lagrangian:

$$\mathcal{H} = \frac{1}{2} g^{\alpha\beta} P_\alpha P_\beta. \tag{75}$$

$$\mathcal{H} = \frac{1}{2} (g^{tt} P_t^2 + g^{\rho\rho} P_\rho^2 + g^{\phi\phi} P_\phi^2 + g^{zz} P_z^2). \tag{76}$$

After calculation, we can obtain four expressions of covariance, which are, respectively:

$$P_t = g_{tt} \dot{t} = -U^{-2} \dot{t} \tag{77}$$

$$P_\rho = g_{\rho\rho} \dot{\rho} = U^2 \dot{\rho} \tag{78}$$

$$P_\phi = g_{\phi\phi} \dot{\phi} = U^2 \rho^2 \dot{\phi} \tag{79}$$

$$P_z = g_{zz} \dot{z} = U^2 \dot{z}. \tag{80}$$

Due to the symmetry of the metric time and coordinates, the relationship between contravariant and covariant metrics becomes very simple. They are reciprocal of each other. The components of the metric tensor are the only diagonal elements that are non-zero. The contravariant metric is obtained as follows:

$$g^{tt} = -U^2 \tag{81}$$

$$g^{\rho\rho} = U^{-2} \tag{82}$$

$$g^{\phi\phi} = U^{-2} \rho^{-2} \tag{83}$$

$$g^{zz} = U^{-2}. \tag{84}$$

By plugging in the calculated contravariant metric and covariance, we can accurately obtain the Hamiltonian of the test particle in TBH space-time:

$$\mathcal{H} = \frac{1}{2} (-U^2 E^2 + U^{-2} P_\rho^2 + U^{-2} \rho^{-2} L^2 + U^{-2} P_z^2). \tag{85}$$

With the Hamiltonian, we can directly write the Hamiltonian equation:

$$\frac{dx^\alpha}{d\tau} = \frac{\partial \mathcal{H}}{\partial p_\alpha}, \quad \frac{dp_\alpha}{d\tau} = -\frac{\partial \mathcal{H}}{\partial x^\alpha}. \tag{86}$$

By substituting the space-time coordinates, we can obtain 8 ordinary differential equations of first order, which are, respectively:

$$\frac{dt}{d\tau} = \frac{\partial \mathcal{H}}{\partial p_t} = g^{tt} P_t, \quad \frac{dp_t}{d\tau} = -\frac{\partial \mathcal{H}}{\partial t} = 0. \tag{87}$$

By combining the two first-order differential equations in Formula (86), a second-order motion equation can be obtained:

$$\ddot{t} = 0. \tag{88}$$

$$\frac{d\rho}{d\tau} = \frac{\partial \mathcal{H}}{\partial p_\rho} = g^{\rho\rho} P_\rho, \quad \frac{dp_\rho}{d\tau} = -\frac{\partial \mathcal{H}}{\partial \rho}. \tag{89}$$

In the same way:

$$\ddot{\rho} = -g^{\rho\rho} \frac{\partial \mathcal{H}}{\partial \rho}. \tag{90}$$

$$\frac{d\phi}{d\tau} = \frac{\partial \mathcal{H}}{\partial p_\phi} = g^{\phi\phi} P_\phi, \quad \frac{dp_\phi}{d\tau} = -\frac{\partial \mathcal{H}}{\partial \phi}. \tag{91}$$

$$\ddot{\phi} = 0. \tag{92}$$

$$\frac{dz}{d\tau} = \frac{\partial \mathcal{H}}{\partial p_z} = g^{zz} P_z, \quad \frac{dp_z}{d\tau} = -\frac{\partial \mathcal{H}}{\partial z}. \tag{93}$$

$$\ddot{z} = -g^{zz} \frac{\partial \mathcal{H}}{\partial z}. \tag{94}$$

Because of the equivalence of Hamiltonian mechanics and Lagrangian mechanics, (19) (20) and (75) (76) must be equivalent. Combining the conservation of energy and the normalization of four velocities, we can obtain: $\mathcal{L} = -\frac{1}{2}$ and $\mathcal{H} = -\frac{1}{2}$. Here, $\mathcal{L} = \mathcal{H}$ can be derived from the Legendre transformation in mathematics, or can be explained in physics, because both \mathcal{L} and \mathcal{H} represent only the same energy, and the deeper reason is that gravity is geometrized, and the potential energy terms in both \mathcal{L} and \mathcal{H} are 0.

2.5. Horizon of Space-Time

TBH space-time is a Riemannian space-time with a sign difference of +2. In this kind of space-time similar to a Minkowski space-time with an indefinite metric, it is possible to have a special hypersurface. Now let us examine whether TBH space-time has an event horizon, that is, a zero surface that preserves space-time symmetry. First of all, let us define a zero hypersurface. Now, let us assume that

$$f(x^\mu) = f(x^1, x^2, x^3, x^4) = 0, \mu = 1, 2, 3, 4. \tag{95}$$

Is a three-dimensional hypersurface in four-dimensional space-time, where the normal vector is defined as

$$n_\mu = \frac{\partial f}{\partial x^\mu}. \tag{96}$$

The length of the normal vector is defined as:

$$n_\mu n^\mu = g^{\mu\nu} n_\mu n_\nu = g^{\mu\nu} \frac{\partial f}{\partial x^\mu} \frac{\partial f}{\partial x^\nu}. \tag{97}$$

If the following conditions are satisfied:

$$g^{\mu\nu} \frac{\partial f}{\partial x^\mu} \frac{\partial f}{\partial x^\nu} = 0. \tag{98}$$

Then the surface is a zero hypersurface whose normal vector length is zero. TBH space-time is statically axisymmetric, and the horizon, as a surface preserving the symmetry of space-time, should also be statically spherically symmetric. Therefore, if the TBH space-time horizon exists, its hypersurface expression $f(x^\mu)$ should be independent of t and ϕ ,

and can only be a function of ρ . Substituted into the TBH space-time metric, the following equation can be obtained:

$$g^{\rho\rho} \left(\frac{\partial f}{\partial \rho}\right)^2 + g^{zz} \left(\frac{\partial f}{\partial z}\right)^2 = 0 \tag{99}$$

$$U^{-2} \left(\left(\frac{\partial f}{\partial \rho}\right)^2 + \left(\frac{\partial f}{\partial z}\right)^2\right) = 0. \tag{100}$$

This is obvious $\left(\frac{\partial f}{\partial \rho}\right)^2 \neq 0, \left(\frac{\partial f}{\partial z}\right)^2 \neq 0$. Therefore, we can only obtain: $U^{-2} = 0$.

The solutions of Equation (100) are three points corresponding to the spatial coordinates of the three black holes, respectively, that is to say, the zero hypersurface of TBH is three points, and the space-time has no horizon.

2.6. One-Dimensional Effective Potential

Different initial values have different orbits. Here, we simplify the problem. We mainly discuss the motion of the particles to be measured on the TBH space-time symmetry plane ($z = 0, \dot{z} = 0$), which can be divided into three orbits: bound state, scattering state and absorption state. The orbit type and total energy of the particles, and the relativity of the particles on the symmetry plane are closely related to the effective potential $V(\rho, a)$. Here, we fix $a = 10$. Firstly, according to the normalized relationship, energy conservation and angular momentum conservation, the following relationship can be obtained:

$$\dot{\rho}^2 + \dot{z}^2 + V = E^2. \tag{101}$$

E is the total energy per unit of the static mass (the sum of the static energy and kinetic energy) that a static observer at infinity can obtain when observing a particle locally. For a unit static mass particle that exists at infinity, $E1$ (moving particle $E > 1$, stationary particle $E = 1$); for unit static-mass particles located in the gravitational field, E is the total energy including gravitational potential energy (the sum of static energy, kinetic energy and gravitational potential energy), E is a conserved quantity on geoid $r(\tau)$. L is the equivalent angular momentum per unit static mass of the particle, $\phi(\tau)$ is the conserved quantity. Here, we obtain the expression of the effective potential:

$$V(\rho, z; L^2) = \frac{L^2}{\rho^2 U^4} + \frac{\kappa}{U^2}. \tag{102}$$

Because ($z = 0, \dot{z} = 0$), we know $\dot{z} = 0$ from the equation of motion. Now, fixed angular momentum $L = 5$, for time-like particle $\kappa = 1$, we can obtain the relationship between the effective potential and radius:

$$V(\rho, 0, 10, 5) = \frac{25}{\rho^2 U^4} + \frac{1}{U^2}. \tag{103}$$

Figure 1 fixed the angular momentum parameter $L = 5$, making the separation distance parameter $a = 0, 3, 5, 8$. Observe the change of the effective potential with a single variable ρ . Figure 2 fixes the separation distance $a = 7$, making angular momentum $L = 0, 1, 2 \dots 10$. Observe the change of the effective potential with a single variable L . As ρ goes to infinity, it is clear from the two diagrams that the relativistic effective goes to 1, and the Newtonian potential of a free particle at infinity from the gravitational source should be equal to zero, and we usually specify that the Newtonian potential at infinity is equal to zero, and that is where the relativistic effective potential is different from the Newtonian potential. Since we take $c = 1, m = 1$ per unit mass, and the total energy of a free class particle at infinity is its rest energy, according to Einstein’s equation of mass and energy, we can very well explain why relativistic efficiency tends to number 1, whether it is changing the angular momentum or changing the separation distance. When ρ is 0 in the effective potential

energy expression, it corresponds to the effective energy of the photon. Now, take $a = 0$ and the angular momentum L as 1, 4, 8, 12, 16, respectively, and the effective energy of a single RN black hole with a mass of 3 can be obtained, as shown in Figure 3:

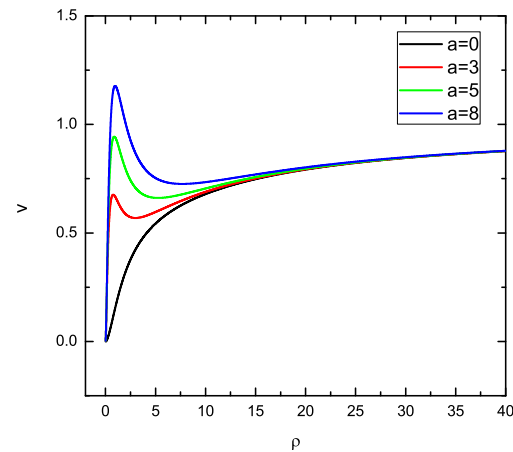


Figure 1. This is a one-dimensional effective potential image of the test particle on the $\rho - z$ plane. Since this is a special case ($L = 5$), we observe it by changing the angular momentum. The different values of a are given: $a = 0, a = 3, a = 5, a = 8$.

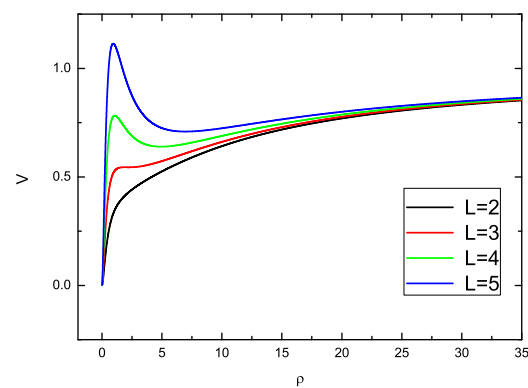


Figure 2. This is a one-dimensional effective potential image of the test particle on the $\rho - z$ plane. Since this is a special case $a = 7$, we observe it by changing the angular momentum. The different values of L are given: $L = 2, L = 3, L = 4, L = 5$.

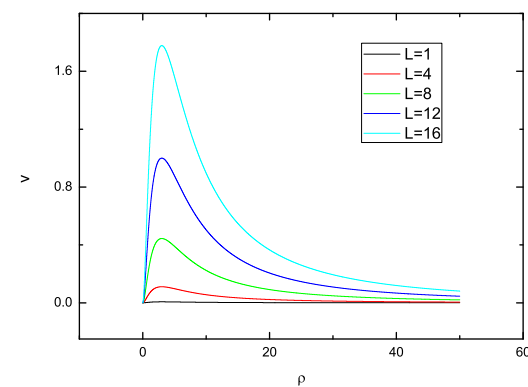


Figure 3. This is a one-dimensional effective potential image of the photons on the $\rho - z$ plane. Since this is a special case ($a = 0$), we observe it by changing the angular momentum. The different values of L are given: $L = 1, L = 4, L = 8, L = 12, L = 16$.

It is not difficult to find that the peak of the effective potential energy increases with the increase of L , and it can also be seen that the photon energy at infinity is 0, corresponding to the residual energy of the photon. When the separation parameter $a = 7$, other conditions remain unchanged, and only the angular momentum is changed, as shown in Figure 4:

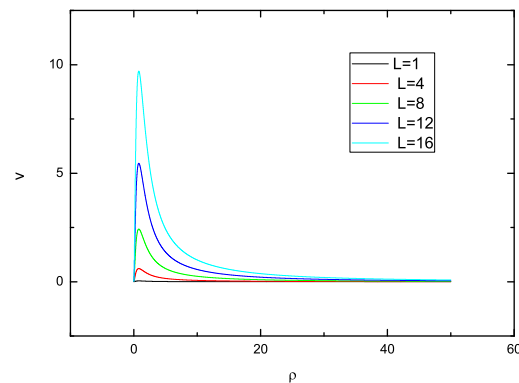


Figure 4. This is a one-dimensional effective potential image of the photons on the $\rho - z$ plane. Since this is a special case ($a = 7$), we observe it by changing the angular momentum. The different values of L are given: $L = 1, L = 4, L = 8, L = 12, L = 16$.

First of all, we can obtain the same rule as Figure 5. Secondly, we find that when the angular momentum is constant, the effective potential energy will increase more obviously with the increase of a .

Now, we classify the time-like free particle motion orbits with different energies in symmetric plane motion with an angular momentum of 6 and separation distance of 5. First, we give its effective potential diagram:

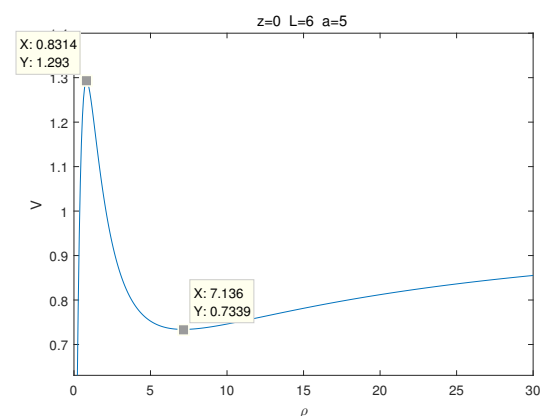


Figure 5. We obtain an image of the effective potential in this case, in which $z = 0, L = 6, a = 5$.

We find that the curve of the potential function has two stationary points, which can be obtained by the partial derivative of the potential function equal to zero and marked in the graph. The conditions are as follows:

$$V_{\rho} = 0. \quad (104)$$

After calculation, we obtain the value of stagnation point as $\rho_1 = 0.8314, \rho_2 = 7.136$, respectively. The corresponding effective potential is $V_1 = 1.293, V_2 = 0.7339$ respectively. Now, let us classify the possible orbits of this particle. (1) If $E^2 > V_1$, then if the particle starts to move away from the black hole, the particle will continue to move towards infinity. If the particle starts to move towards the black hole, the particle will eventually fall into the black hole. (2) If $E^2 = V_1$, then the particle moves in an unstable circular orbit. In other words, if the particle is disturbed inward, the particle will no longer move in a circular orbit,

but will spiral into the black hole. If the particle is disturbed outward, the particle will run to infinity. (3) If $1 \leq E^2 < V_1$, the particle is in a scattering state. No matter whether the particle starts out in a direction towards or away from the black hole, the particle ends up heading for infinity. (4) If $V_2 < E^2 < 1$, the particle is in a bound state, and the particle moves in an elliptical orbit. (5) If $E^2 = V_2$, then the particle moves in a stable circular orbit, that is, any small disturbance will not make the particle deviate from the circular orbit, and the particle will eventually continue to move in a circular orbit. (6) If $E^2 < V_2$, obviously, at this point the particle can only fall into the black hole, regardless of its initial state.

3. The Effect of M_1M_2 on the Equilibrium Position

We found that when the $M_1 = M_2$ on the z axis of radius equal to 0, $z = 0$ is a balance, but here there is a black hole, we generally do not consider the situation, no matter whether for photon M_1 or M_2 , how for quality, there is no balance, but for class particles there is such a point, and the premise is the angular momentum from 0. We first study the $M_1:M_2 = 2:1$, and draw the effective potential along with the change of z , $\rho = 0$, $a = 5$, $L = 7$.

$$V_{\text{eff}}(z) = \frac{1}{2U^2(z)} \tag{105}$$

$$U(\rho = 0, z) = 1 + \frac{1}{((z - 5)^2)^{\frac{1}{2}}} + \frac{1}{((z + 5)^2)^{\frac{1}{2}}} + \frac{1}{(z^2)^{\frac{1}{2}}}. \tag{106}$$

According to Formula (18), we adjust the mass ratio $M_2:M_1 = 1:1, 3:1, 5:1, 7:1, 1:3, 1:5, 1:7$, respectively, and draw the picture as shown in Figure 6:

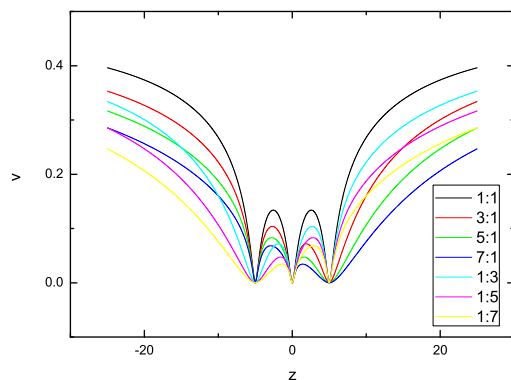


Figure 6. We give the effective potential at different mass ratios of black holes on the z -axis.

It is clear from the graph that there is a stable equilibrium point at $z = 0$, but there is a black hole, so it is not necessary to discuss stability here. We also found that there is an unstable equilibrium point between 0 and 5 and 0 and -5 , and when the mass ratio changes, we find that the equilibrium point changes, always in favor of the small mass black hole. Now, let us look at the separation distance between the black holes when the masses are the same a pair, and the effective potential is the effect of the energy curve.

It can be seen from Figure 7 that the change of separation distance a does not change the shape of the effective potential. The separation distance a of V_z only changes the peak value. When the value of a is relatively small, the equilibrium position of the effective potential is small. When the value of a is relatively large, the equilibrium position of the effective potential is higher. The reason is very simple. Similar to Newtonian mechanics, the lifted object has gravitational potential energy. When the separation distance a is larger, it is equivalent to the higher the object is lifted, the greater the gravitational potential energy will be, so the effective potential peak here will also become larger.

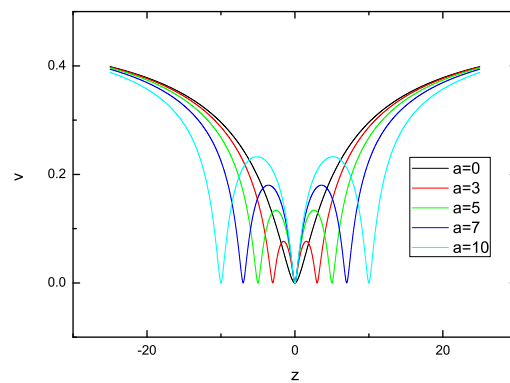


Figure 7. We obtain the effective potential for different separation distances at the same mass, which $a = 0, 3, 5, 7, 10$.

4. The Stability of Symmetric Plane Orbits is Discussed by Phase Plane Analysis

Now the orbital stability on the symmetric plane is analyzed by the method of phase plane analysis. Now, the orbital stability on the symmetric plane is analyzed by the method of phase plane analysis. Now, select the plane $z = 0$, and Formula (101) can be written as:

$$\dot{\rho}^2 = E^2 - V, \quad (107)$$

Due to the

$$\dot{\rho} = \frac{d\rho}{d\phi} \frac{d\phi}{d\tau} = \frac{d\rho}{d\phi} \dot{\phi}. \quad (108)$$

Combined with Equation (91), the following equation can be obtained:

$$\dot{\rho} = \frac{d\rho}{d\phi} \frac{L}{\rho^2 U^2}. \quad (109)$$

Therefore, (109) can be rewritten as:

$$\left(\frac{d\rho}{d\phi}\right)^2 = \frac{\rho^4 U^4}{L^2} (E^2 - V). \quad (110)$$

Then we perform the transformation $R = \frac{1}{\rho}$, $dR = d\rho^{-1}$

$$\left(\frac{dR}{d\phi}\right)^2 = \frac{U^4(R)}{L^2} (E^2 - V(R)). \quad (111)$$

Among them:

$$U(R) = 1 + \frac{2}{\sqrt{\frac{1}{R^2} + a^2}} + R. \quad (112)$$

$$V(R) = \frac{R^2 L^2}{U^4(R)} + \frac{\kappa}{U^2 R}. \quad (113)$$

Now we are going to do the last transformation $x = R$ $y = \frac{dR}{d\phi}$

$$y^2 = \frac{U^4(x)}{L^2} (E^2 - V(x)). \quad (114)$$

When theta $\frac{dR}{d\phi} = 0$, we can define a new effective potential Y .

$$Y = 1 + \frac{U^4(x)}{L^2(E^2 - V(x))}. \tag{115}$$

When $\frac{dY}{dx} = 0$, the particle’s trajectory is circular. When the trajectory of the particle is a stable circular orbit, this condition needs to be met:

$$\frac{dY^2}{dx^2} \geq 0. \tag{116}$$

5. Stability Conditions for Test Particle Circular Orbit in TBH Space-Time

We study time-like particles that move in a circular motion on a symmetric plane, which needs to satisfy these conditions: (1) $z = 0$. (2) The radius and ordinate of the circular orbit of the particle do not change with proper time $\dot{\rho} = \dot{z} = 0$. Obviously, the acceleration term should also be equal to 0, (3) $\ddot{\rho} = \ddot{z} = 0$. From this, we can derive:

$$V_z = 0 \tag{117}$$

$$V_\rho = 0. \tag{118}$$

where $V_i = \partial_i V (i = z, \rho)$. Hence, the circular orbits are realized at stationary points of V where the values of V are positive. After simplification, we can obtain these equations:

$$U_z = 0 \tag{119}$$

$$U_\rho = -\frac{\rho}{(\rho^2 + z^2)^{\frac{3}{2}}} - \frac{\rho}{(\rho^2 + (z - a)^2)^{\frac{3}{2}}} - \frac{\rho}{(\rho^2 + (z + a)^2)^{\frac{3}{2}}}. \tag{120}$$

$$L^2 = L_0^2(\rho, z) := -\frac{\rho^3 U^2 U_\rho}{U + 2\rho U_\rho}. \tag{121}$$

$$E^2 = E_0^2(\rho, z) := V(\rho, z; L_0^2). \tag{122}$$

Here, we require that the square of angular momentum is greater than 0, so the effective potential energy must also be greater than 0. Finally, we find that the particle’s motion along the circular orbit needs to meet the following requirements: $U_z = 0, L^2 = L_0^2 \geq 0$, and $E^2 = E_0^2$. Then we analyze the stability of the circular orbit. According to the stability analysis theory, if the effective potential of the circular orbit is at a minimum, we call it a stable circular orbit. When the effective potential is at the local maximum or saddle point, we call it unstable circular orbit. In order to determine whether the circular orbit is stable, we need to introduce the Hessian matrix, whose matrix elements are as follows: $V_{ij} = \partial_i \partial_j V$, and then define the determinant and trace of the Hessian matrix :

$$h(\rho, z; L^2) = \det V_{ij} = V_{\rho\rho} V_{zz} - V_{\rho z} V_{z\rho} \tag{123}$$

$$k(\rho, z; L^2) = \text{Tr } V_{ij} = V_{\rho\rho} + V_{zz}. \tag{124}$$

According to the above definition, we now summarize the stability analysis of circular orbits as follows : (1) A circular orbit is stable at a stagnation point of V is equivalent to $h > 0$ and $k > 0$. (2) A circular orbit is unstable at a stagnation point of V is equivalent to $h > 0$ and $k < 0$, or $h < 0$. When a stable circular orbit sequence becomes an unstable circular orbit sequence at a certain radius, we call the circular orbit at this radius an edge-stable circular orbit, and V has an inflection point (i.e., $h = 0$). It is worth noting that we call

the smallest edge stable circular orbit the innermost stable circular orbit. In the rest of the article, we study the circular orbits of equal mass $M_1 = M_2 = M_3$ in TBH spacetime. We use units of $M_i = 1, i = 1, 2, 3$. In this particular case, Equation (119) can be simplified as :

$$\frac{2a - 2z}{2(\rho^2 + (a - z)^2)^{\frac{3}{2}}} - \frac{2a + 2z}{2(\rho^2 + (a + z)^2)^{\frac{3}{2}}} - \frac{z}{(\rho^2 + (z)^2)^{\frac{3}{2}}} = 0. \tag{125}$$

Now, we define the trace and determinant of the Hessian matrix that satisfies the circular orbit:

$$h_0(\rho, z) = h(\rho, z; L_0^2) \Big|_{U_z=0} \tag{126}$$

$$k_0(\rho, z) = k(\rho, z; L_0^2) \Big|_{U_z=0}. \tag{127}$$

From this, we can infer the region of motion in the circular orbit of the example:

$$D = \{(\rho, z) | h_0 > 0, k_0 > 0, L_0^2 > 0\}. \tag{128}$$

The feasible region of D when $a = 5$ is given as Figure 8:

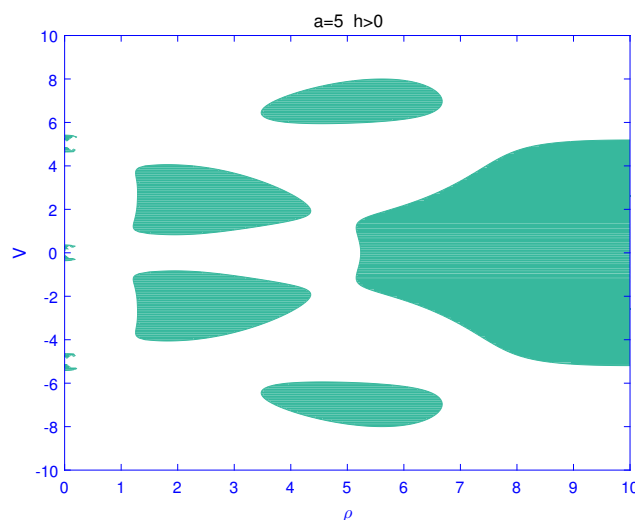


Figure 8. The stable circular orbital interval satisfies $a = 5$.

6. Coordinate Quantities and Intrinsic Quantities in TBH Spacetime

6.1. Coordinate Distance and Proper Distance

TBH space-time is orthogonal to the time axis, that is:

$$g_{0i} = 0, i = 1, 2, 3. \tag{129}$$

We know that the simultaneous plane can be established and the unified coordinates can be determined in space-time. According to the orthogonality of the time axis, the expression of space distance is as follows:

$$dl^2 = \gamma_{ik} dx^i dx^k \tag{130}$$

$$\gamma_{ik} = g_{ik} - \frac{g_{0k}g_{0i}}{g_{00}}. \tag{131}$$

Simplify to the following formula

$$dl^2 = g_{ik} dx^i dx^k. \tag{132}$$

Now, write the proper distance expression in the three directions of ρ, ϕ, z :

$$dl_\rho = U d\rho \tag{133}$$

$$dl_\phi = U \rho d\phi \tag{134}$$

$$dl_z = U dz. \tag{135}$$

It can be seen from the three expressions (133)–(135) that the coordinate distance is not equal to the proper distance. There is an additional proportional function U , which is a function of the space-time point. In other words, the three coordinate distances have no measurement significance.

6.2. Coordinate Time and Proper Time

Now, the observer at rest with respect to a coordinate system x^μ is investigated to find the relationship between its coordinate time and proper time:

$$\begin{aligned} d\tau &= \frac{ids}{c} = \frac{\sqrt{-g_{\mu\nu}dx^\mu dx^\nu}}{c} \\ &= \frac{\sqrt{-g_{00}dx^0}}{c} = \sqrt{-g_{00}}dt. \end{aligned} \tag{136}$$

By combining Equations (11) and (12):

$$d\tau = U^{-1}dt. \tag{137}$$

Thus, it can be seen that proper time and coordinate time are also separated by a proportional function except for the case of infinity, where the value of the function is equal to 1 and the coordinate time is equal to proper time. Therefore, TBH space-time coordinate time is generally not of measurement significance. Because the time axis is orthogonal, TBH space-time can establish a unified coordinate time, so that the coordinates of all points in space-time are the same. It can be seen from the above formula that within the same coordinate time interval, standard clocks at different points in space-time will travel through different proper times.

6.3. The Natural Velocity of Light and the Coordinate Velocity of Light

The radial velocity and tangential velocity of light in TBH space-time are now discussed. Suppose the tangential natural velocity of the photon at any point in TBH space-time is:

$$v_\tau = \frac{dl_\tau}{d\tau} = \frac{U\rho d\phi + Udz}{d\tau}. \tag{138}$$

The radial natural velocity is:

$$v_\rho = \frac{dl_\rho}{d\tau} = \frac{Ud\rho}{d\tau}. \tag{139}$$

For a photon its space time interval is zero:

$$ds^2 = \frac{-dt^2}{U^2} + U^2\rho^2d\phi^2 + U^2dz^2 = 0 \tag{140}$$

$$ds^2 = \frac{-dt^2}{U^2} + U^2d\rho^2 = 0. \tag{141}$$

Thus, it can be obtained that:

$$v_\rho = v_\tau = 1. \tag{142}$$

Obviously, the tangential and radial natural velocities are both c . Therefore, at any point in the TBH space-time, the measured speed of light is independent of the direction of light. As with Minkowski, the speed of light in TBH space-time is still isotropic. In order to calculate the coordinate light speed of TBH space-time, the following definition is given. The radial coordinate light speed can be defined as:

$$v_{c\rho} = \frac{d\rho}{dt} = U^{-1}. \tag{143}$$

The tangential coordinate speed of light can be defined as:

$$v_{c\tau} = \frac{dl_\tau}{dt} = U. \tag{144}$$

It can be found that the radial coordinate velocity is equal to the speed of light at infinity, but it can be much less than the speed of light near the three black holes, and the tangential coordinate velocity is also equal to the speed of light at infinity, but it can be much more than the speed of light near the three black holes. Visible coordinate speed of light anisotropy. Now, we multiply Equations (143) and (144), and we are surprised to find that the product of tangential and radial coordinate velocities is exactly equal to the speed of light squared:

$$v_{c\tau}v_{c\rho} = 1^2. \tag{145}$$

This equation reflects the conservation of energy in a certain sense. However, the coordinate speed of light is only a formal definition, so there is no practical significance, of practical significance is the proper speed of light, which can be verified by experimental detection.

6.4. Red Shift in TBH Space-Time

Because the TBH space-time metric is time independent, that is:

$$\frac{\partial g_{\mu\nu}}{\partial t} = 0, \mu, \nu = 0, 1, 2, 3. \tag{146}$$

And satisfying (146), we can say that TBH spacetime is steady-state. We now discuss the standard time in stationary space-time. It is assumed that there are two points A and B in space-time, which are a stationary light source and stationary observer, respectively. The light source at A emits an optical signal at coordinate time t_1 , and the observer at B receives the optical signal at coordinate time t_2 . The coordinate difference is:

$$\delta t = t_2 - t_1. \tag{147}$$

Then, the light source at A emits an optical signal at coordinate time t'_1 , and the coordinate when the signal is received at B is t'_2 . The coordinate difference is:

$$\delta t' = t'_2 - t'_1. \tag{148}$$

In the TBH space-time, there is no time coordinate t , which satisfies the Equation (146), so the space-time is stable. We can infer that the time difference between the two coordinates must be equal:

$$\delta t = \delta t'. \tag{149}$$

This is equivalent to:

$$t_2 - t_1 = t'_2 - t'_1. \tag{150}$$

Then, the following relation can be obtained:

$$dt_2 \equiv t_2 - t_1 \tag{151}$$

$$dt_1 \equiv t'_2 - t'_1 \tag{152}$$

$$dt_1 = dt_2. \tag{153}$$

where dt_1 is the coordinate time difference between the two optical signals at A , and dt_2 is the coordinate time difference between the two optical signals at B . The relationship between them and their own inherent time is:

$$d\tau_1 = \sqrt{-g_{00}(A)} = dt_1 \tag{154}$$

$$d\tau_2 = \sqrt{-g_{00}(B)} = dt_2. \tag{155}$$

Thus, the proper time relationship between A and B can be obtained:

$$d\tau_2 = \frac{\sqrt{-g_{00}(B)}}{\sqrt{-g_{00}(A)}} d\tau_1. \tag{156}$$

Now suppose: $U(A) > U(B)$, According to Formula (5), we can obtain:

$$d\tau_2 = \frac{U(A)}{U(B)} d\tau_1. \tag{157}$$

Where the gravitational potential is high, proper time moves slowly, while where the gravitational potential is low, proper time moves fast. When B takes infinity, $U(B)$ approaches 1, and we can obtain:

$$d\tau_2 = dt = U(A)^2 d\tau_1. \tag{158}$$

Atomic clocks at two different locations in space-time cannot be compared directly, but the frequency of light can still be used to verify the change in proper time. The spectral lines emitted by atoms have an inherent frequency, which reflects some natural vibration frequency of atoms. The vibration of atoms can be regarded as a metronome, N is the number of times the metronome vibrates. Its frequency is:

$$\nu = \frac{dN}{d\tau}. \tag{159}$$

According to the same number of atomic vibration in A and B , it can be obtained that:

$$dN_1 = dN_2, \nu_1 d\tau_1 = \nu_2 d\tau_2. \tag{160}$$

Combined with Formulas (158) and (159), the following equation can be obtained:

$$\nu_2 = \frac{\sqrt{-g_{00}(A)}}{\sqrt{-g_{00}(B)}} \nu_1. \tag{161}$$

$$\nu_2 = \frac{U(B)}{U(A)} \nu_1. \tag{162}$$

It is clear that where the gravitational potential is low, the light frequency is low, and if we assume that B goes to infinity then $U(B)$ goes to 1, that is a much more obvious conclusion:

$$\nu = \frac{1}{U(A)}\nu_0. \quad (163)$$

ν_0 is the photon frequency near the black hole, ν is the frequency measured by the observer at the infinite distance, the fundamental reason is that the standard clock at different time and space points moves at different speeds.

7. The Order and Chaos Orbits of Particle

In order to describe the order and chaos of particles, two methods are used to determine whether particles are in order or chaos. One method is the Poincare cross section method. If the Poincare interface is a closed curve with no intersection point, then the orbit is in order; if the Poincare interface diagram has scattered points, then the orbit is chaotic. The other is the Fast Lyapunov Indicator (FLI), in which the fast Lyapunov Indicator formula is as follows:

$$FLI = \log_{10} \frac{d(\tau)}{d(0)}. \quad (164)$$

If the FLI curve increases exponentially, then the particle orbit is chaotic; if it grows slowly, then the particle orbit is orderly. If the two methods are used together, the order and chaos of particles can be judged more clearly. Now, we study under a set of determined parameters, $a = 30$, $E = 0.98$, $L = 7$, $M1 = M2 = M3 = 1$, $r = 46$, $pr = 0.1$, $z = 0$, and $pz = 0.2$. Using the RK algorithm of order 8 (9) to solve the space-time regular equation, we can obtain the Lyapunov exponential graph and Poincare cross section graph as follows:

As can be seen from Figure 9a,b, FLI rises rapidly and the scattered points of the Poincare cross-section are obvious. Therefore, we can determine that under this initial condition, we find the chaotic orbit of the particle, which can also be seen from the two-dimensional space projection of the particle, as shown in Figure 9c.

When the initial position r is not at the same time has a great influence on the particle's chaotic sex, on the basis of the above parameters, makes the $r = 50$, as can be seen from Figure 10a, the FLI agreed slow growth, present the linear growth, while in the Poincare section Figure 10b shows a closed elliptical orbit, combining space projection Figure 10c we found that the projection is orderly orbit, so we found an orderly track, and the result in changes of the particle's chaotic orbit is the initial position of r .

The change of the separation distance a of the three static distribution black holes also affects the chaos of the particle orbit. Now, take $a = 20$, and the graph is as follows.

According to the diagram, it can be clearly seen that the FLI agreed on in Figure 11a rises faster, but in Figure 9a, the rising speed is slower, the scatter distribution is not obvious, but the outgoing scatter curve is crossed. Combined with the trajectory of the test particle in Figure 9c, it can be judged that the trajectory of the test particle becomes smaller, and the test particle is still a chaotic orbit under the same conditions, but the chaos is weak. As a becomes smaller, let us see what happens to the orbital chaos of the test particles. Now take $a = 5$, as shown in Figure 12:

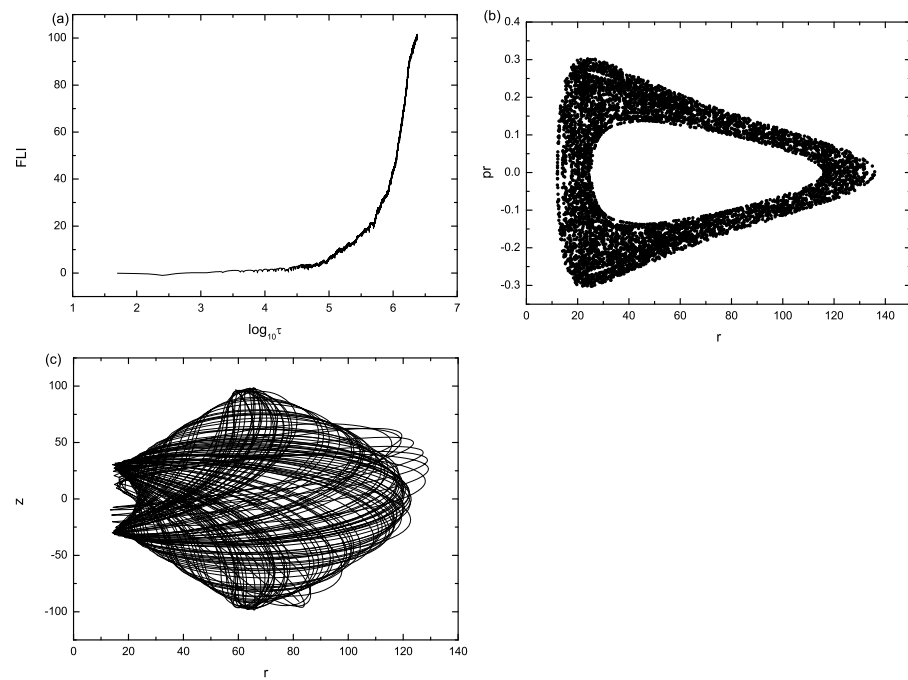


Figure 9. (a) is the fast Lyapunov index diagram, (b) is the Poincare section, and (c) is the spatial trajectory projection. Which $a = 30$, $E = 0.98$, $L = 7$, $M1 = M2 = M3 = 1$, $r = 46$, $pr = 0.1$, $z = 0$, $pz = 0.2$.

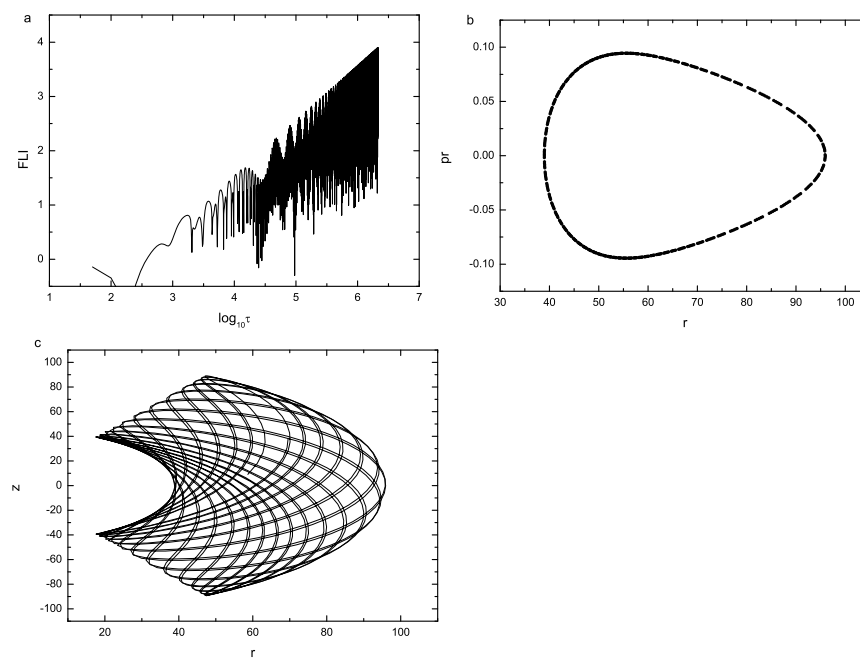


Figure 10. (a) is the Fast Lyapunov Index diagram, (b) is the Poincare section, and (c) is the spatial trajectory projection. Which $a = 30$, $E = 0.98$, $L = 7$, $M1 = M2 = M3 = 1$, $r = 50$, $pr = 0.1$, $z = 0$, $pz = 0.2$.

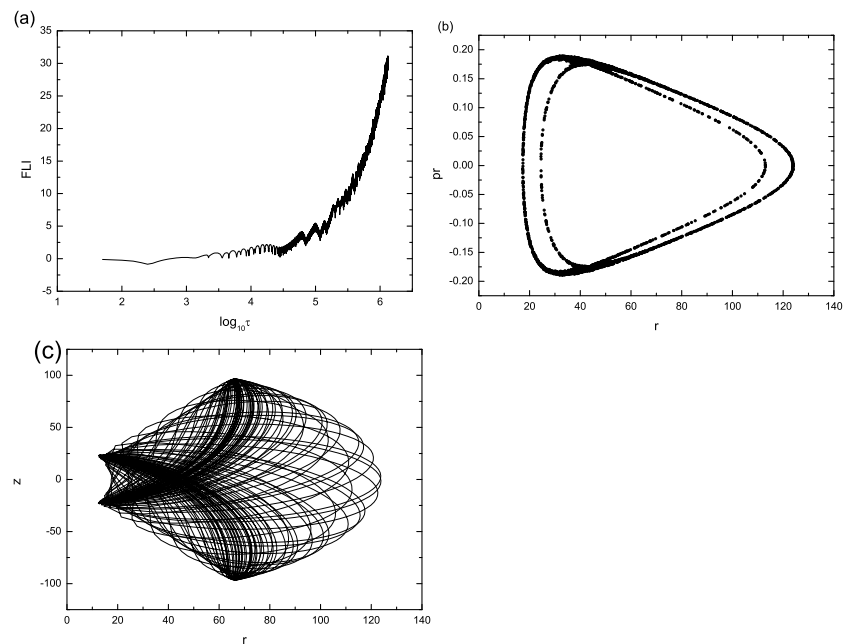


Figure 11. (a) is the Fast Lyapunov Index diagram, (b) is the Poincare section, and (c) is the spatial trajectory projection. Which $a = 20$, $E = 0.98$, $L = 7$, $M1 = M2 = M3 = 1$, $r = 46$, $pr = 0.1$, $z = 0$, $pz = 0.2$.

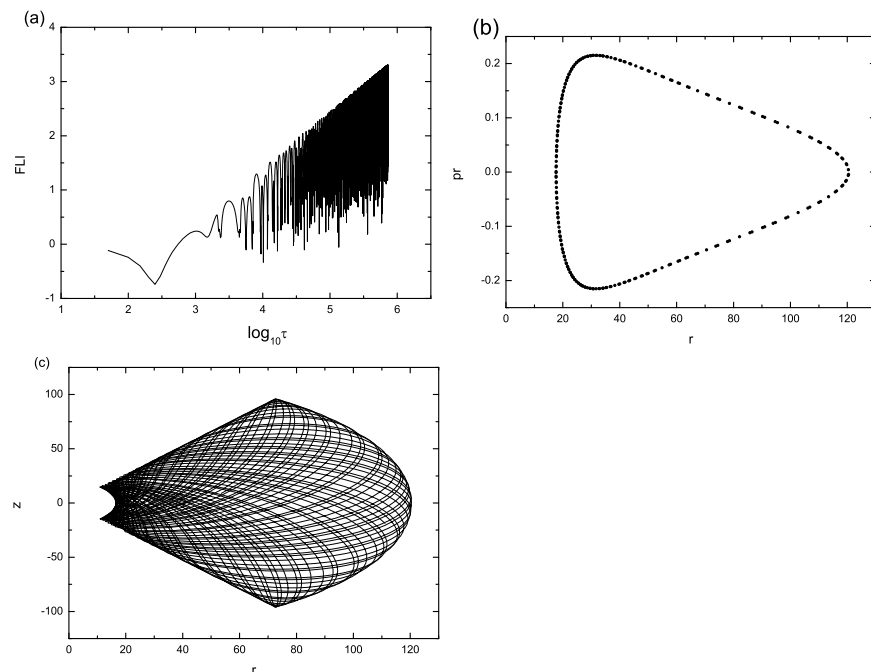


Figure 12. (a) is the Fast Lyapunov Index diagram, (b) is the Poincare section, and (c) is the spatial trajectory projection. Which $a = 5$, $E = 0.98$, $L = 7$, $M1 = M2 = M3 = 1$, $r = 46$, $pr = 0.1$, $z = 0$, $pz = 0.2$.

It is obvious that FLI rises slowly rather than exponentially in Figure 12a. Looking at the Poincare cross-section in Figure 12b, it is a closed curve. Combined with the projection trajectory in Figure 12c, it can be concluded that this particle orbit is an ordered orbit. That is to say that when a is a small value, the particle's orbit goes from chaotic to ordered.

Now let's select another set of determined parameters $a = 100$, $E = 0.98$, $L = 7$, $M1 = M2 = M3 = 1$, $r = 60$, $pr = 0.1$, $z = 0$, $pz = 0.1$ for discussion. The figure is as follows: Figure 13,

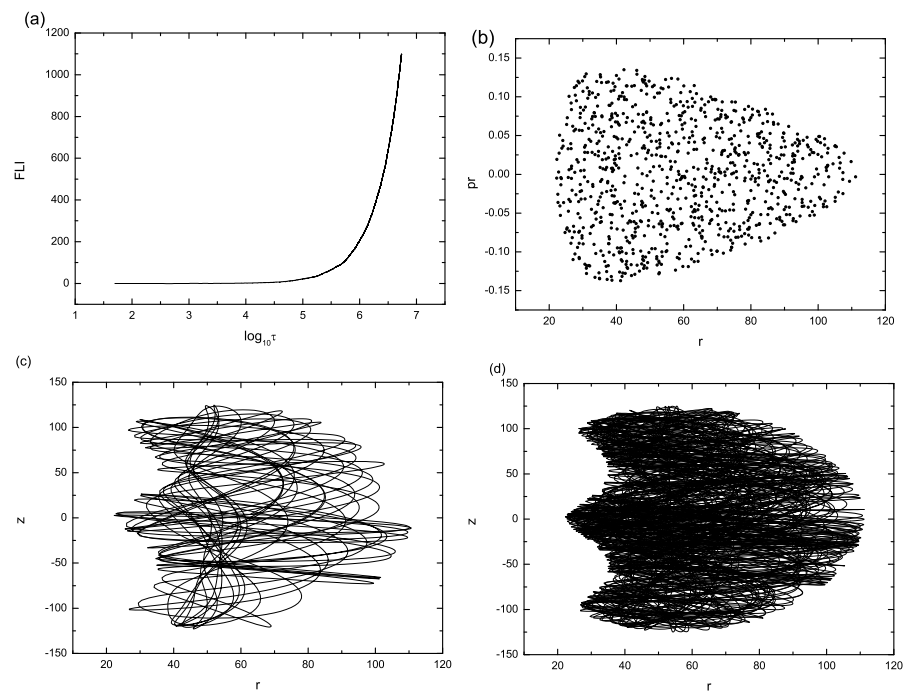


Figure 13. (a) is the Fast Lyapunov Index diagram, (b) is the Poincaré section, (c) is the spatial trajectory projection, (d) is a long time space projection. Which $a = 100$, $E = 0.98$, $L = 7$, $M1 = M2 = M3 = 1$, $r = 60$, $pr = 0.1$, $z = 0$, $pz = 0.1$.

According to Figure 13a, it can be seen that the FLI agreed explosive growth, Poincaré Figure 13b a scatter scattered, and can be seen from the two track projection particle movement desultorily, trajectory Figure 13c,d, respectively, for a short time and long time integral effect, it can be seen that the longer the particle movement, the more chaos, thus it can be concluded that this type of chaos is strong!

Then, what changes will be brought by changing the initial position R of the particle in the case of strong chaos? Now select $r = 30, 40, 50, 60, 70, 80$, and make Figure 14 as follows:

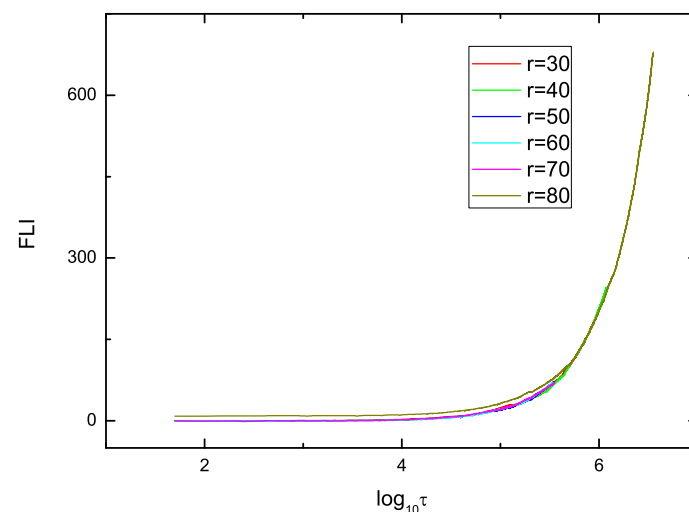


Figure 14. This is the fast Lyapunov index diagram, which $a = 100$, $E = 0.98$, $L = 7$, $M1 = M2 = M3 = 1$, $r = 30, 40, 50, 60, 70, 80$, $pr = 0.1$, $z = 0$, $pz = 0.1$.

According to Figure 14 FLI alone, it can be seen that the growth pattern of the FLI curve is almost the same even if the initial position R of the tested particle is different. Therefore, it can be judged that the change of initial position R has almost no influence on

the chaos of the particle under strong chaos. Next, we will discuss whether the change of A under the above determined parameters can influence the chaos of the particle. Now, take $a = 20, 50, 100$ and draw the figure as follows.

According to Figure 15 FLI, the growth rate of FLI becomes slow with the decrease of a , so it can be inferred that the orbital chaos of the test particle weakens with the decrease of a .

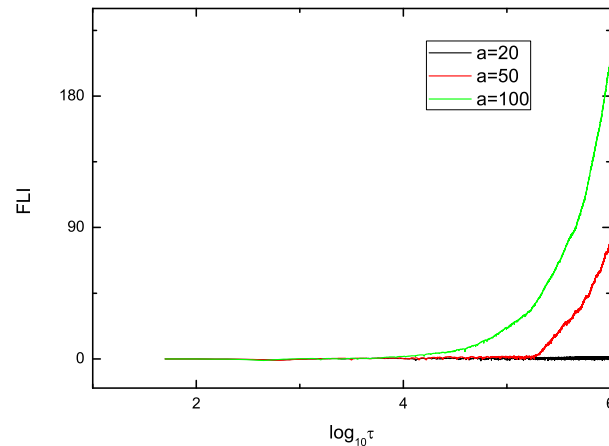


Figure 15. This is the fast Lyapunov index diagram, in which $a = 20, 50, 100$, $E = 0.98$, $L = 7$, $M1 = M2 = M3 = 1$, $r = 60$, $pr = 0.1$, $z = 0$, $pz = 0.1$.

Then, we test whether the energy change of particles will have an impact on chaos. Now we choose $a = 7$, $L = 4.8$, $M1 = M2 = M3 = 1$, $r = 38$, $pr = 0.1$, $z = 0$ and $pz = 0.1$ for discussion. Take the energy $E = 0.95, 0.96, 0.97$ and 0.98 as the figure below.

It can be seen from Figure 16 that when the energy is 0.95 , the Poincare cross-section is a closed blue curve, indicating that this is an ordered orbit. When the energy is 0.96 , the red curve is no longer closed and scattered points appear, and weak chaos has been generated. Look at the Figure 17 again now, when the energy is 0.95 , the FLI agreed indicators were not puffed up, also indicates the orderly orbit, but when energy increase to 0.96 , the red FLI agreed in a significantly upward curve, as $E = 0.97, 0.98$, and became warped on the more obvious, at this time as the chaotic orbits, combined with the Poincare section and the FLI, which agreed to a qualitative description when the experimental particle energy increases, the particle tracks may vary from order to chaos.

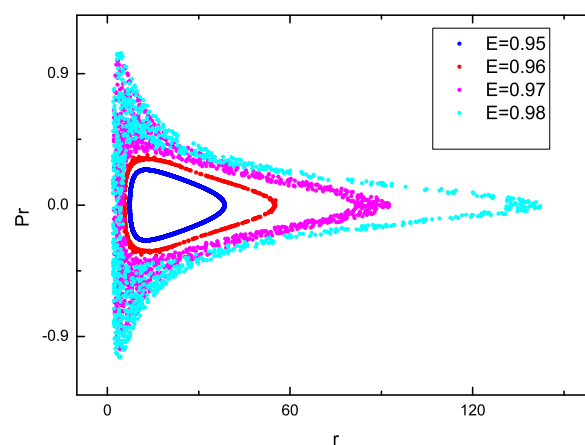


Figure 16. This is the Poincare section, in which $a = 7$, $E = 0.95, 0.96, 0.97, 0.98$, $L = 4.8$, $M1 = M2 = M3 = 1$, $r = 38$, $pr = 0.1$, $z = 0$, $pz = 0.1$.

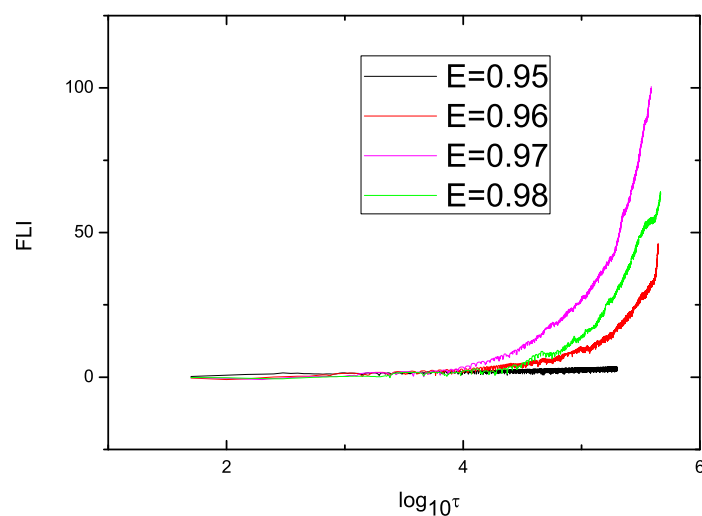


Figure 17. This is the fast Lyapunov index diagram, in which $a = 7$, $E = 0.95, 0.96, 0.97, 0.98$, $L = 4.8$, $M_1 = M_2 = M_3 = 1$, $r = 38$, $pr = 0.1$, $z = 0$, $pz = 0.1$.

8. Conclusions

We study the space-time properties of the TBH, including giving the space-time metric, calculating the Christoffel symbol, and the Riemann curvature tensor, which facilitates our further understanding and research on the TBH curved space-time. For the TBH space-time horizon, we reach the conclusion that the space-time has no horizon, and the three exposed singular points are located at the coordinates of the three black holes, which are $z = 0$, $-a$, a , (see Equation (100)), respectively. The relationship between the coordinate quantity and the intrinsic quantity and the redshift expression in space-time are also given (see Equation (161)). On the analysis of the effective potential of the test particles moving in the three static black holes, we reach some qualitative conclusions. The peak value of the effective potential energy increases with the increase of a and L , and the mass also has a great influence on the effective potential energy of the plane with $\rho = 0$. This is similar to Newton's potential energy balance, in which the side of the celestial body mass increases, and the equilibrium point will tend to this side. In the future, we will analyze the two-dimensional effective potential energy of the particles in more detail, which is more convenient for us to study the more general motion trajectory of the test particles. We give the stability condition of the particle's circular orbit motion in the symmetric plane by the phase plane analysis method, and then use the Hessian matrix to further analyze the two-dimensional effective potential of the particle, and give the stability condition of the particle's circular orbit in space. Finally, the numerical calculation is used to explore the order and chaos of the test particles in space-time (see Figures 12 and 13). It is found that the initial energy of the experimental particles is the main factor affecting the chaos of the particles. Most of the test particles with low energy are in an ordered orbit. When the energy increases, the particle orbit will move from order to chaos (see Figures 16 and 17). In future research, we hope to study TBH space-time more deeply.

Author Contributions: Formal analysis, G.S.; Resources, X.S.; Writing—original draft, Y.W. All authors have read and agreed to the published version of the manuscript.

Funding: This research received no external funding.

Data Availability Statement: No new data were created or analyzed in this study. Data sharing is not applicable to this article.

Conflicts of Interest: The authors declare no conflict of interest.

References

1. Abbott, B.P.; Abbott, R.; Abbott, T.D.; Abernathy, M.R.; Acernese, F.; Ackley, K.; Adams, C.; Adams, T.; Addesso, P.; Adhikari, R.X.; et al. Observation of Gravitational Waves from a Binary Black Hole Merger. *Phys. Rev. Lett.* **2016**, *116*, 061102. [[CrossRef](#)] [[PubMed](#)]
2. Abbott, B.P.; Abbott, R.; Abbott, T.D.; Abernathy, M.R.; Acernese, F.; Ackley, K.; Adams, C.; Adams, T.; Addesso, P.; Adhikari, R.X.; et al. Properties of the Binary Black Hole Merger GW150914. *Phys. Rev. Lett.* **2016**, *116*, 241102. [[CrossRef](#)] [[PubMed](#)]
3. Abbott, B.P.; Abbott, R.; Abbott, T.D.; Acernese, F.; Ackley, K.; Adams, C.; Adams, T.; Addesso, P.; Adhikari, R.X.; Adya, V.B.; et al. Multi-messenger observations of a binary neutron star merger. *Astrophys. J. Lett.* **2017**, *848*, L12. [[CrossRef](#)]
4. Abbott, B.P.; Abbott, R.; Abbott, T.; Abraham, S.; Acernese, F.; Ackley, K.; Adams, C.; Adhikari, R.X.; Adya, V.B.; Affeldt, C.; et al. GWTC-1: A Gravitational-Wave Transient Catalog of Compact Binary Mergers Observed by LIGO and Virgo During the First and Second Observing Runs. *Phys. Rev. X* **2019**, *9*, 031040. [[CrossRef](#)]
5. Weyl, H. The theory of gravitation. *Ann. Phys.* **1917**, *359*, 117. [[CrossRef](#)]
6. Majumdar, S.D. A class of exact solutions of Einstein's field equations. *Phys. Rev.* **1947**, *72*, 390. [[CrossRef](#)]
7. Papaetrou, A. A static solution of the equations of the gravitational field for an arbitrary charge distribution. *Proc. R. Ir. Acad. Sect. A* **1947**, *51*, 191.
8. Hartle, J.B.; Hawking, S.W. Solutions of the Einstein-Maxwell equations with many black holes. *Commun. Math. Phys.* **1972**, *26*, 87. [[CrossRef](#)]
9. Kramer, D.; Neugebauer, G. The superposition of two Kerr solutions. *Phys. Lett. A* **1980**, *75*, 259. [[CrossRef](#)]
10. Nitta, D.; Chiba, T.; Sugiyama, N. Shadows of colliding black holes. *Phys. Rev. D* **2011**, *84*, 063008. [[CrossRef](#)]
11. Bohn, A.; Throwe, W.; Hébert, F.; Henriksson, K.; Bunandar, D.; Scheel, M.A.; Taylor, N.W. What does a binary black hole merger look like? *Class. Quantum Gravity* **2015**, *32*, 065002. [[CrossRef](#)]
12. Patil, M.; Mishra, P.; Narasimha, D. Curious case of gravitational lensing by binary black holes: A tale of two photon spheres, new relativistic images and caustics. *Phys. Rev. D* **2017**, *95*, 024026. [[CrossRef](#)]
13. Assumpcao, T.; Cardoso, V.; Ishibashi, A.; Richartz, M.; Zilhao, M. Black hole binaries: Ergoregions, photon surfaces, wave scattering, and quasinormal modes. *Phys. Rev. D* **2018**, *98*, 064036. [[CrossRef](#)]
14. Cunha, P.V.P.; Herdeiro, C.A.R.; Rodriguez, M.J. Shadows of exact binary black holes. *Phys. Rev. D* **2018**, *98*, 044053. [[CrossRef](#)]
15. Psaltis, Dimitrios and Talbot, Colm and Payne, Ethan and Mandel, Ilya, Probing the black hole metric: Black hole shadows and binary black-hole inspirals. *Phys. Rev. D* **2021**, *103*, 106036
16. Campanelli, M.; Dettwyler, M.; Hannam, M.; Lousto, C.O. Relativistic three-body effects in black hole coalescence. *Phys. Rev. D* **2006**, *74*, 087503. [[CrossRef](#)]
17. Torigoe, Y.; Hattori, K.; Asada, H. Gravitational Wave-forms for Two- and Three-Body Gravitating Systems. *Phys. Rev. Lett.* **2009**, *102*, 251101. [[CrossRef](#)] [[PubMed](#)]
18. Seto, N. Relativistic resonant relations between massive black hole binary and extreme mass ratio inspiral. *Phys. Rev. D* **2012**, *85*, 064037. [[CrossRef](#)]
19. Yamada, K.; Asada, H. Nonchaotic evolution of triangular configuration due to gravitational radiation reaction in the three-body problem. *Phys. Rev. D* **2016**, *93*, 084027. [[CrossRef](#)]
20. Hayasaki, K.; Mineshige, S.; Sudou, H. Binary black hole accretion flows in merged galactic nuclei. *Publ. Astron. Soc. Jpn.* **2007**, *59*, 427. [[CrossRef](#)]
21. Kimitake, H.; Mineshige, S.; Ho, L.C. A supermassive binary black hole with triple disks. *Astrophys. J.* **2008**, *682*, 1134.
22. Novikov, I.D.; Thorne, K.S. Astrophysics of black holes. In *Black Holes (Les Astres Occus)*; DeWitte, C., DeWitt, B., Eds.; Gordon and Breach: New York, NY, USA, 1973; p. 343.
23. Clark, J.P.A.; Eardley, D.M. Evolution of close neutron star binaries. *Astrophys. J.* **1977**, *215*, 311. [[CrossRef](#)]
24. Kidder, L.E.; Will, C.M.; Wiseman, A.G. Coalescing binary systems of compact objects to (post)5/2-Newtonian order. III. Transition from inspiral to plunge. *Phys. Rev. D* **1993**, *47*, 3281. [[CrossRef](#)]
25. Penrose, R. Chandrasekhar, black holes, and singularities. *J. Astrophys. Astron.* **1996**, *17*, 213–231. [[CrossRef](#)]
26. Contopoulos, G. Periodic Orbits and Chaos around Two Fixed Black Holes. *Proc. R. Soc. A* **1990**, *413*, 183–202.
27. Contopoulos, G. Periodic Orbits and Chaos around Two Fixed Black Holes. II. *Proc. R. Soc. A* **1991**, *435*, 551–562.
28. Wunsch, A.; Muller, T.; Weiskopf, D.; Wunner, G. Circular orbits in the extreme Reissner-Nordström dihole metric. *Phys. Rev. D* **2013**, *87*, 024007. [[CrossRef](#)]
29. Camps, J.; Hadar, S.; Manton, N.S. Exact gravitational wave signatures from colliding extreme black holes. *Phys. Rev. D* **2017**, *96*, 061501. [[CrossRef](#)]
30. Igata, T.; Ishihara, H.; Takamori, Y. Constants of motion for constrained Hamiltonian systems: A particle around a charged rotating black hole. *Phys. Rev. D* **2011**, *83*, 047501. [[CrossRef](#)]
31. Igata, T.; Ishihara, H.; Takamori, Y. Stable Bound Orbits of Massless Particles around a Black Ring. *Phys. Rev. D* **2013**, *87*, 104005. [[CrossRef](#)]
32. Wald, R. *General Relativity*; University Chicago Press: Chicago, IL, USA, 1984.
33. Ellis, J.; Fairbairn, M.; Hütsi, G.; Raidal, M.; Urrutia, J.; Vaskonen, V.; Veermäe, H. Prospects for Future Binary Black Hole GW Studies in Light of PTA Measurements. *arXiv* **2013**, arXiv:2301.13854.

34. Abbott, B.P.; Abe, H.; Acernese, F.; Ackley, K.; Adhicary, S.; Adhikari, N.; Adhikari, R.X.; Adkins, V.K.; Adya, V.B.; Affeldt, C.; et al. Observation of gravitational waves from a 22-solar-mass bi-nary black hole coalescence. *Phys. Rev. Lett.* **2016**, *116*, 241103. [[CrossRef](#)] [[PubMed](#)]
35. Shakura, N.I.; Sunyaev, R.A. Black holes in binary systems. Observational appearance. *Astron. Astrophys.* **1973**, *24*, 337–355.
36. Page, D.N.; Thorne, K.S. Disk-accretion onto a black hole. Time-averaged structure of accretion disk. *Astrophys. J.* **1974**, *191*, 499–506. [[CrossRef](#)]
37. Chandrasekhar, S.; Thorne, K.S. The mathematical theory of black holes. *Int. Ser. Monogr. Phys.* **1985**, *53*, 1013. [[CrossRef](#)]
38. Pugliese, D.; Quevedo, H.; Ruffini, R. Circular motion of neutral test particles in Reissner-Nordstrom spacetime. *Phys. Rev. D* **2011**, *83*, 024021. [[CrossRef](#)]
39. Bardeen, J.M.; Press, W.H.; Teukolsky, S.A. Rotating Black Holes: Locally Nonrotating Frames, Energy Extraction, and Scalar Synchrotron Radiation. *Astrophys. J.* **1972**, *178*, 347. [[CrossRef](#)]
40. Liu, C.-Y.; Lee, D.-S.; Lin, C.-Y. Geodesic motion of neutral particles around a Kerr-Newman black hole. *Class. Quantum Gravity* **2017**, *34*, 235008. [[CrossRef](#)]
41. Misner, C.W.; Thorne, K.S.; Wheeler, J.A.; Kaiser, D.I. *Gravitation*; Princeton University Press: Princeton, NJ, USA, 2017.
42. Pugliese, D.; Quevedo, H.; Ruffini, R. Equatorial circular motion in Kerr space-time. *Phys. Rev. D* **2011**, *84*, 044030. [[CrossRef](#)]
43. Faraji, S. Circular Geodesics in a New Generalization of q-Metric. *Universe* **2022**, *8*, 195. [[CrossRef](#)]
44. Narayan, R.; McClintock, J.E. Observational evidence for a correlation between jet power and black hole spin. *Mon. Not. R. Astron. Soc. Lett.* **2012**, *419*, L69–L73. [[CrossRef](#)]
45. Tchekhovskoy, A.; Narayan, R.; McKinney, J.C. Efficient generation of jets from magnetically arrested accretion on a rapidly spinning black hole. *Mon. Not. R. Astron. Soc. Lett.* **2011**, *418*, L79–L83. [[CrossRef](#)]
46. Zahrani, A.M.A. Escape of charged particles moving around a weakly magnetized Kerr black hole. *Phys. Rev. D* **2014**, *90*, 044012. [[CrossRef](#)]
47. Abdujabbarov, A.; Ahmedov, B. Charged particle motion around rotating black hole in braneworld immersed in magnetic field. *Phys. Rev. D* **2010**, *81*, 044022. [[CrossRef](#)]
48. Akcay, S.; Barack, L.; Damour, T.; Sago, N. Gravitational self-force and the effective-one-body formalism between the innermost stable circular orbit and the light ring. *Phys. Rev. D* **2012**, *86*, 104041. [[CrossRef](#)]
49. Asano, K.; Maszros, P. Ultrahigh-energy cosmic ray production by turbulence in gamma-ray burst jets and cosmogenic neutrinos. *Phys. Rev. D* **2016**, *94*, 023005. [[CrossRef](#)]
50. Cabanac, C.; Fender, R.P.; Dunn, R.J.H.; Koerding, E.G. On the variation of black hole accretion disc radii as a function of state and accretion rate. *Mon. Not. R. Astron. Soc. Lett.* **2009**, *396*, 1415. [[CrossRef](#)]
51. Campanelli, M.; Lousto, C.O.; Zlochower, Y. The last orbit of binary black holes. *Phys. Rev. D* **2006**, *73*, 061501. [[CrossRef](#)]
52. Chakraborty, C. Inner-most stable circular orbits in extremal and non-extremal Kerr-Taub-NUT spacetimes. *Eur. Phys. J. C* **2014**, *74*, 2759. [[CrossRef](#)]
53. Delsate, T.; Rocha, J.V.; Santarelli, R. Geodesic motion in equal angular momenta Myers-Perry-AdS spacetimes. *Phys. Rev. D* **2015**, *92*, 084028. [[CrossRef](#)]
54. Hadar, S.; Kol, B.; Berti, E.; Cardoso, V. Comparing numerical and analytical calculations of post-ISCO ringdown amplitudes. *Phys. Rev. D* **2011**, *84*, 047501. [[CrossRef](#)]
55. Harms, E.; Lukes-Gerakopoulos, G.; Bernuzzi, S.; Nagar, A. Spinning test body orbiting around a Schwarzschild black hole: Circular dynamics and gravitational-wave fluxes. *Phys. Rev. D* **2016**, *94*, 104010. [[CrossRef](#)]
56. Hod, S. Analytic toy model for the innermost stable circular orbit shift. *Phys. Rev. D* **2013**, *87*, 024036. [[CrossRef](#)]
57. Hod, S. Self-gravitating ring of matter in orbit around a black hole: The innermost stable circular orbit. *Eur. Phys. J. C* **2014**, *74*, 2840. [[CrossRef](#)]
58. Isoyama, S.; Barack, L.; Dolan, S.R.; Tiec, A.L.; Nakano, H.; Shah, A.G.; Tanaka, T.; Warburton, N. Gravitational self-force correction to the innermost stable circular equatorial orbit of a Kerr black hole. *Phys. Rev. Lett.* **2014**, *113*, 161101. [[CrossRef](#)]
59. Lukes-Gerakopoulos, G.; Harms, E.; Bernuzzi, S.; Nagar, A. Spinning test-body orbiting around a Kerr black hole: Circular dynamics and gravitational-wave fluxes. *Phys. Rev. D* **2017**, *96*, 064051. [[CrossRef](#)]
60. Zaslavskii, O.B. Innermost stable circular orbit near dirty black holes in magnetic field and ultra-high energy particle collisions. *Eur. Phys. J. C* **2015**, *75*, 403. [[CrossRef](#)]
61. Shiose, R.; Kimura, M.; Chiba, T. Motion of charged particles around a weakly magnetized rotating black hole. *Phys. Rev. D* **2014**, *90*, 124016. [[CrossRef](#)]
62. Hussain, S.; Hussain, I.; Jamil, M. Dynamics of a charged particle around a slowly rotating Kerr black hole immersed in magnetic field. *Eur. Phys. J. C* **2014**, *74*, 3210. [[CrossRef](#)]
63. Takahashi, M.; Koyama, H. Chaotic motion of charged particles in an electromagnetic field surrounding a rotating black hole. *Astrophys. J.* **2009**, *693*, 472–485. [[CrossRef](#)]
64. Frolov, V.P.; Shoom, A.A. Motion of charged particles near weakly magnetized Schwarzschild black hole. *Phys. Rev. D* **2010**, *82*, 084034. [[CrossRef](#)]
65. Frolov, V.P. Weakly magnetized black holes as particle accelerators. *Phys. Rev. D* **2012**, *85*, 024020. [[CrossRef](#)]
66. Pugliese, D.; Quevedo, H.; Ruffini, R. Equatorial circular orbits of neutral test particles in the Kerr-Newman spacetime. *Phys. Rev. D* **2013**, *88*, 024042. [[CrossRef](#)]

67. Corinaldesi, E.; Papapetrou, A. Spinning test particles in general relativity. II. *Proc. R. Soc. Lond. Ser. A* **1951**, *209*, 259–268.
68. Rasband, S. Black holes and spinning test bodies. *Phys. Rev. Lett.* **1973**, *30*, 111. [[CrossRef](#)]
69. Tod, K.P.; de Felice, F.; Calvani, M. Spinning test particles in the field of a black hole. *Nuovo C. B Ser.* **1976**, *34*, 365. [[CrossRef](#)]
70. Zhang, Y.-P.; Wei, S.-W.; Guo, W.-D.; Sui, T.-T.; Liu, Y.-X. Innermost stable circular orbit of spinning particle in charged spinning black hole background. *Phys. Rev. D* **2018**, *97*, 084056. [[CrossRef](#)]
71. Schroven, K.; Hackmann, E.; Lämmerzahl, C. Relativistic dust accretion of charged particles in Kerr-Newman spacetime. *Phys. Rev. D* **2017**, *96*, 063015. [[CrossRef](#)]
72. Zhang, M.; Jiang, J.; Liu, Y.; Liu, W.-B. Collisional Penrose process of charged spinning particles. *Phys. Rev. D* **2018**, *98*, 044006. [[CrossRef](#)]

Disclaimer/Publisher’s Note: The statements, opinions and data contained in all publications are solely those of the individual author(s) and contributor(s) and not of MDPI and/or the editor(s). MDPI and/or the editor(s) disclaim responsibility for any injury to people or property resulting from any ideas, methods, instructions or products referred to in the content.